Recycling spent LiNi$_{1-x-y}$Mn$_x$Co$_y$O$_2$ cathodes to bifunctional NiMnCo catalysts for zinc-air batteries

Miaolun Jiao[a,1], Qi Zhang[a,1], Chenliang Ye[b,1], Zhibo Liu[c], Xiongwei Zhong[a], Junxiong Wang[a], Chuang Li[a], Lixin Dai[a], Guangmin Zhou[a,2], and Hui-Ming Cheng[a,c,d,2]

The skyrocketing production of lithium-ion batteries (LIBs) for electric vehicles portends that tremendous numbers of used LIBs will be generated. However, the recycling of used LIBs is limited by the complicated separation processes of traditional pyrometallurgy and hydrometallurgy methods. Here, we applied a rapid thermal radiation method to convert spent LiNi$_{1-x-y}$Mn$_x$Co$_y$O$_2$ (NMC) cathodes from used LIBs into highly efficient NiMnCo-based catalysts for zinc-air batteries (ZABs) through acid leaching and radiative heating processes, which avoids sophisticated separation of different metals and can synthesize the catalysts rapidly. The prepared NiMnCo-activated carbon (NiMnCo-AC) catalyst presents a unique core-shell structure, with face-centered cubic Ni in the core and spinel NiMnCoO$_4$ in the shell, which redistributes the electronic structure of the NiMnCoO$_4$ shell to decrease the energy barrier for oxygen reduction reaction (ORR)/oxygen evolution reaction (OER) processes and ensures high electrocatalytic activities. The NiMnCo-AC catalyst in ZABs as cathode materials exhibits a high power density of 187.7 mW cm^{-2}, low voltage gap of 0.72 V at the initial three cycles, and long cycling duration of 200 h at the current density of 10 mA cm^{-2}. This work provides a promising strategy to recycle spent LIBs to highly efficient catalysts for ZABs.

spent NMC cathode | rapid thermal radiation | NiMnCo nanoparticles | core-shell structure | zinc-air batteries

The worldwide trend of developing electric vehicles largely increases the demand for lithium-ion batteries (LIBs), which causes the price of related metals (e.g., Li, Ni, Co, and Mn) to soar and generates millions of tons of used LIBs (1–4). The large amount of LIBs waste leads to serious environmental pollution (5–7). To alleviate the environmental problems and mitigate the shortage of related metals, it is of critical importance to recycle these metals from spent LIBs (8–11). LiNi$_{1-x-y}$Mn$_x$Co$_y$O$_2$ (NMC)-type cathodes are largely used in LIBs due to their high energy density and good electrochemical stability; therefore, bountiful Li, Ni, Mn, and Co metals in spent NMC cathodes can be recovered (12–14). Transition metals (e.g., Ni, Mn, and Co) usually exhibit promising bifunctional oxygen reduction reaction (ORR)/oxygen evolution reaction (OER) performance (15–17). As one of the most promising energy storage devices, zinc-air batteries (ZABs) need the ORR/OER in the cathode side, which calls for low-cost bifunctional catalysts as cathode materials (18–20). Thus, converting the NMC scraps into highly efficient NiMnCo-based catalyst cathodes for ZABs can not only alleviate environmental pollution, but also significantly reduce the cost of ZABs.

Various strategies have been proposed to recover Ni, Mn, and Co from spent NMC cathodes, among which typical pyrometallurgy and hydrometallurgy methods are commonly used (21–23). Pyrometallurgy smelts the spent cathode materials in a blast furnace at high temperatures to produce transition metal alloys, followed by multistep purification and separation processes (24, 25). Hydrometallurgy dissolves the metals through an acid leaching process and separates the transition metals by subsequent extraction and precipitation steps (26–28). However, both the pyrometallurgy and hydrometallurgy methods involve multistep separation processes of the transition metals, which largely increases the difficulty in recycling the NMC cathode, leading to low recovery efficiency and high recovery cost (29, 30). To avoid the complicated separation processes, methods of directly converting cathode scraps into highly efficient catalysts have been pursued (31, 32). It is verified that the layered lithium transition metal oxides (typical cathode materials in LIBs) exhibit improved catalytic activity of OER after the delithiation process (33–36). In addition, with the modification of Ni, the spent LiFePO$_4$ cathode presents high OER performance because of the in situ evolution of Ni-LiFePO$_4$ active materials (16). Even though the spent cathode materials can be used as catalysts after modification, the large particle size limits their applications in

Author affiliations: [a]Shenzhen Geim Graphene Center, Tsinghua-Berkeley Shenzhen Institute & Tsinghua Shenzhen International Graduate School, Tsinghua University, Shenzhen 518055, China; [b]Department of Chemistry, Tsinghua University, Beijing 100084, China; [c]Shenyang National Laboratory for Materials Science, Institute of Metal Research Chinese Academy of Sciences, Shenyang 110016, China; and [d]Institute of Technology for Carbon Neutrality, Shenzhen Institute of Advanced Technology, Chinese Academy of Sciences, Shenzhen 518055, China

[1]M.J., Q.Z., and C.Y. contributed equally to this work.

[2]To whom correspondence may be addressed. Email: guangminzhou@sz.tsinghua.edu.cn or hmcheng@sz.tsinghua.edu.cn.

ORR, and they are rarely studied in ZABs as cathode materials. Therefore, it is important to directly convert NMC cathodes into nanosized catalysts to improve the bifunctional ORR/OER catalytic activities, which makes it possible to use them as cathode materials in ZABs.

Herein, we report a rapid thermal radiation method to synthesize NiMnCo-activated carbon (NiMnCo-AC) catalysts from spent NMC cathodes efficiently. The NiMnCo nanoparticles are determined to be a core-shell structure with face-centered cubic (fcc) Ni in the core and spinel $NiMnCoO_4$ in the shell, which delivers competitive ORR/OER performance in alkaline solutions. Density functional theory (DFT) calculations elucidate that the Ni core induces the redistribution of the electronic structure of the $NiMnCoO_4$ shell, and the $NiMnCoO_4$ shell provides efficient active sites for the ORR/OER processes; therefore, the synergistic effect between the Ni core and the $NiMnCoO_4$ lowers the energy barrier of the rate-determining step. Based on the unique core-shell structure of the NiMnCo-AC cathode, the ZAB exhibits a high discharge capacity of 779 mAh g^{-1} at the high current density of 50 mA cm^{-1}, the low voltage gap of 0.72 V at the initial three cycles, superior cycling stability for 200 h at the current density of 10 mA cm^{-2}, and excellent flexibility to power the light-emitting diode (LED) at a bending state.

Results and Discussion

The NiMnCo-AC catalyst was fabricated by the recycling of NiMnCo from a spent NMC cathode and a following rapid thermal radiation process, as shown in Fig. 1. The spent NMC cathodes were collected from spent LIBs (*SI Appendix*, Fig. S1) and dissolved into nitric acid to obtain a mixed NiMnCo solution. The concentrations of the mixed NiMnCo solution were detected to be 1.73, 0.97, and 0.68 g L^{-1} for Ni, Mn, and Co, respectively, by inductively coupled plasma optical emission spectrometer (ICP-OES), as shown in *SI Appendix*, Fig. S2. The mixed NiMnCo salt was loaded on an active carbon support, and then the obtained NiMnCo-AC precursor was transferred to a carbon cloth and quickly moved across a high-temperature radiative heating zone, as shown in Fig. 1B. The rapid thermal radiation process induces the formation of NiMnCo nanoparticles, while the limited heating time prevents the nanoparticles from growing. Thus, a NiMnCo-AC catalyst was obtained after the rapid thermal radiation, and the NiMnCo nanoparticles were uniformly dispersed on the active carbon. The recovery of NiMnCo mixed solution from NMC scraps combined with the fast radiative heating method promotes the facile and efficient production of NiMnCo-AC catalysts.

The NiMnCo-AC catalyst can be largely produced as black powders with the mass loading of 1.39 wt%, 0.80 wt%, and 0.57 wt% for Ni, Mn, and Co, respectively, and the ratio is consistent with the concentrations of mixed NiMnCo solution (Fig. 2A and *SI Appendix*, Fig. S3). As shown in *SI Appendix*, Fig. S4, the ratio of defective carbon peak to graphitic carbon peak (I_D/I_G) is 1.77 for AC material due to the disordered structure of AC. The NiMnCo-AC sample shows a higher I_D/I_G of 1.95, illustrating that the introduction of metal nanoparticles produced more defective sites on the activated carbon support. According to the Brunauer-Emmett-Teller (BET) analysis in *SI Appendix*, Fig. S5, the specific surface area of NiMnCo-AC catalyst was calculated to be 760 m^2 g^{-1}, which is beneficial to the exposure of active sites on NiMnCo-AC samples. As shown in Fig. 2 B and C, the NiMnCo nanoparticles are well dispersed on the AC, with an average particle size

of 6.38 nm. To determine the electronic structure and local structure of the nanoparticles, X-ray absorption fine structure (XAFS) analysis was carried out on the Ni K edge, Mn K edge, and Co K edge. As displayed in Fig. 2 D–F, the white line intensity and adsorption edge energy of the NiMnCo-AC are higher than those of Ni, Mn, and Co foil, indicating a high valence of Ni, Mn, and Co in the NiMnCo-AC, which results from the formation of metal oxides on the sample. In the Ni K edge R-space extended XAFS (EXAFS), the NiMnCo-AC exhibits a broad scattering peak at ∼2.11 Å, which is close to the scattering peak of Ni foil (Fig. 2G). This result suggests that, in addition to Ni oxide, there are many metallic Ni in the sample. By contrast, in the Mn K edge and Co K edge R-space EXAFS (Fig. 2 H and I), the main scattering peaks are located at ∼1.63 Å and ∼1.56 Å, respectively, which are typical to Mn-O and Co-O scattering, indicating that the main chemical states of Mn and Co species are metal oxides. The k^2-weighted R-space EXAFS of the sample were further fitted. In the Ni K edge fitting results (*SI Appendix*, Table S1 and Fig. S6 A–C), the Ni-Ni coordination number is 4.9 with a bond distance at 2.50 Å, while the Ni-O coordination number is only 2.8 with a bond distance at 2.03 Å. By contrast, in the Mn K edge fitting results (*SI Appendix*, Table S2 and Fig. S6 D–F), the Mn-O coordination number reaches 4.5, while there are only a small number of Mn-M (Ni, Co, Mn) bonds in the first shell. The small number of Mn-M (Ni, Co, Mn) bonds could be attributed to the strong interaction between metal oxides and metallic Ni in the interface. Similar results are also observed in the Co K edge fitting results (*SI Appendix*, Table S3 and Fig. S6 G–I). The Co-O coordination number is 5.1, while the Co-O-M (Ni, Co, Mn) coordination number is only 0.6 in the first shell. In the second shell, the Mn-O-M (Ni, Co, Mn) and Co-O-M (Ni, Co, Mn) bond distances are very close (∼3.0 Å), which could be attributed to the formation of the trimetallic $NiMnCoO_x$ phase in the NiMnCo-AC sample. These results are also confirmed by the wavelet transform (WT). As shown in Fig. 2 J–L, the intensity maxima of the Ni K edge is close to Ni-Ni scattering, confirming the chemical states of Ni species are mainly metallic Ni, while the intensity maxima of Mn K edge and Co K edge are close to Mn-O and Co-O scattering, respectively. The XAFS results indicate that there are two phases existing in the NiMnCo nanoparticles, including metallic Ni and $NiMnCoO_x$.

To further reveal the distribution of Ni and $NiMnCoO_x$ in the nanoparticles, the aberration corrected-scanning transmission electron microscopy (AC-STEM) images of the NiMnCo-AC catalyst were acquired. As shown in Fig. 3 A and B, the Ni, Mn, and Co are well dispersed on the nanoparticles. By analyzing the element distribution of one nanoparticle, the Mn and Co atoms are concentrated in the shell, while Ni atoms are located over the entire nanoparticle, which reveals the fact of the Ni core as well as the $NiMnCoO_x$ shell (Fig. 3C). The core-shell structure could be attributed to the easy reduction of Ni species, while Mn and Co species are very difficult to reduce. In the high-resolution TEM (HRTEM) images (Fig. 3 D and E), the NiMnCo nanoparticles are dispersed on the AC, and the crystal structure in the particle center is confirmed to be Ni (111) orientation. To determine the long-range order structure of the Ni@$NiMnCoO_x$ core-shell nanoparticle, we simulated the X-ray diffusion (XRD) patterns of Ni and $NiMnCoO_x$ based on the identified local structure from EXAFS analysis. As shown in Fig. 3F, the structure type of Ni is fcc, while the $NiMnCoO_x$ is spinel structure ($NiMnCoO_4$). The estimated size of Ni is ∼7.6 nm according to the Debye-Scherrer method (*SI Appendix*, Table S4). Combined with XAFS,
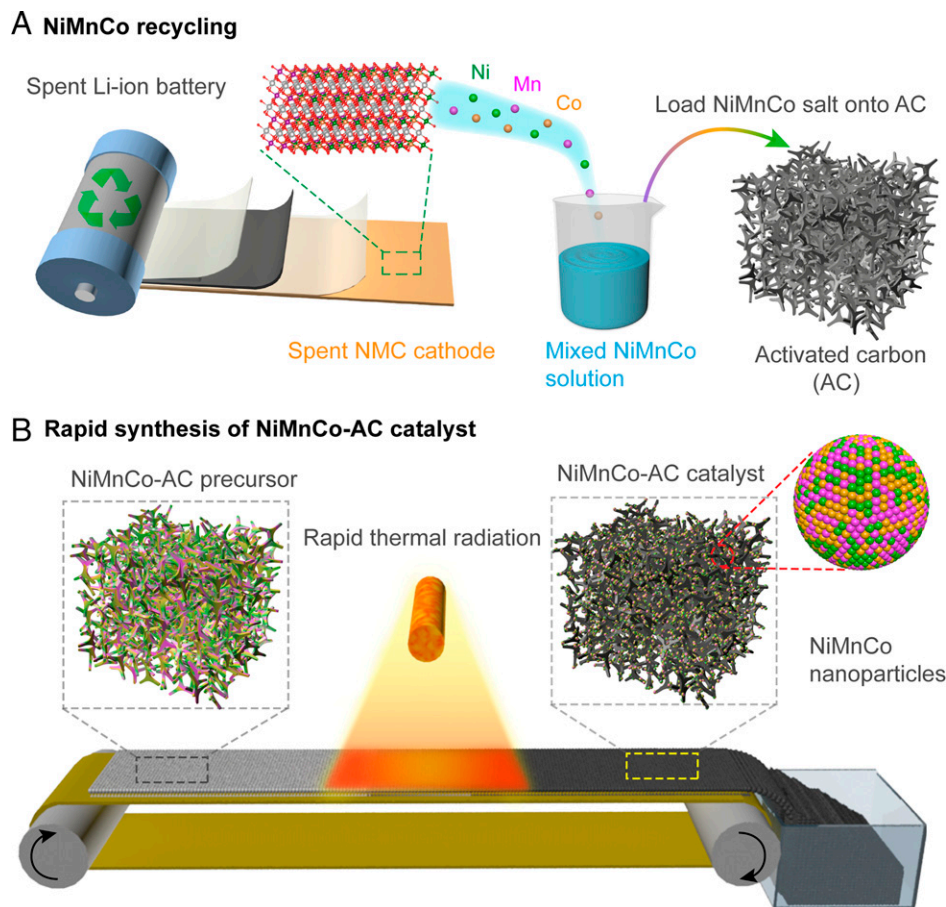
Fig. 1. Schematic of the fabrication process of the NiMnCo-AC catalyst from spent LIBs. (*A*) Recovery of the NiMnCo from spent LIBs. A mixed NiMnCo solution was obtained by dissolving a spent NMC532 cathode in nitric acid. Then, the NiMnCo salt was loaded on AC to prepare a NiMnCo-AC precursor. (*B*) Schematic of the rapid thermal radiation method to synthesize the NiMnCo-AC catalyst continuously. The NiMnCo-AC precursor was driven by a conveyor and moved through a radiative heating zone. After that, NiMnCo nanoparticles were formed and uniformly dispersed on the surface of AC support.

AC-STEM, and XRD analysis, the precise structure of the NiMnCo nanoparticles is identified, which shows a Ni@NiMn-CoO$_4$ core-shell structure, including fcc-structured Ni in the core and spinel NiMnCoO$_4$ in the shell (Fig. 3*G*).

The ORR performance of the Ni@NiMnCoO$_4$ catalyst (named NiMnCo-AC) was evaluated by linear sweep voltammetry curves with the Co-AC, NiMnCoO$_4$-AC, and 5Pt-AC control samples, which were measured on a rotating disk electrode in O$_2$-saturated 0.1 M potassium hydroxide (KOH) solution at a rotating speed of 1,600 revolutions per minute (rpm). The NiMnCo-AC catalyst exhibits an onset potential (E$_0$) of 0.97 V and a half-wave potential (E$_{1/2}$) of 0.82 V, revealing competitive ORR catalytic activity to the 5% Pt-AC catalyst (Fig. 4*A*). The Tafel plots of the Co-AC, NiMnCo-AC, NiMn-CoO$_4$-AC, and 5Pt-AC in Fig. 4*B* were derived from the corresponding ORR curves. The NiMnCo-AC catalyst delivered the low Tafel slope of 68.79 mV dec^{-1}, illustrating the fast catalytic kinetics. As shown in Fig. 4*C*, with the increasing rotating speed from 400 to 2,025 rpm, the limited current densities of the NiMnCo-AC catalyst are gradually increased due to the high ORR efficiency and the faster diffusion of O$_2$ and OH$^-$ at higher rotating speed. According to the rotating ring disk electrode (RRDE) measurements in Fig. 4 *D* and *E*, the NiMnCo-AC catalyst shows the lowest ring current of 0.11 mA cm^{-2}, which corresponds to a low H$_2$O$_2$ yield below ~10% at the potential range of 0.2 to 0.7 V, indicating the high efficiency of ORR. Additionally, the average electron transfer number of the NiMnCo-AC catalyst was calculated to

be 3.8, showing a four-electron pathway during the ORR process. The OER process was conducted in a N$_2$-saturated 1 M KOH solution at the rotating speed of 1,600 rpm. As shown in Fig. 4*F*, the NiMnCo-AC exhibits a low potential of 1.57 V at the current density of 10 mA cm^{-2}, lower than those of commercial IrO$_2$ (1.58 V), NiMnCoO$_4$-AC (1.61 V), and Co-AC (1.63 V) and illustrating the high OER activity of the NiMnCo-AC catalyst.

First-principle DFT calculations were conducted to investigate the enhancement of the catalytic mechanism in OER/ORR for the NiMnCo-AC catalyst (Fig. 4 *G–J*). Based on the analysis results of TEM and XRD, a Ni(111)@NiMnCoO$_4$(110) model was constructed (see *SI Appendix, Experimental Section* for more details). The electronic structure calculations were conducted to show the interlayer electronic-coupling effect between Ni(111) and NiMnCoO$_4$(110). As shown in Fig. 4*G*, after coupling NiMnCoO$_4$(110) with Ni(111), the charge density in the hybrid's interlayer was redistributed with the apparent electrons of conductive Ni(111) transferring to NiMnCoO$_4$(110), leading to an electron-rich region in the NiMnCoO$_4$(110) layer. The localized electron accumulation leads to the appearance of electron states at the Fermi level for the spin-down density of states (DOS), as demonstrated in Fig. 4*H*. This change in DOS for Ni(111)@NiMnCoO$_4$(110) indicates an enhanced electron mobility, which is significant to improve the electrocatalytic performance in ORR/OER. More importantly, on the surface layer of the Ni(111)@NiMnCoO$_4$(110), electrons are primarily localized in Mn atoms and Co atoms, which infers that the Mn and
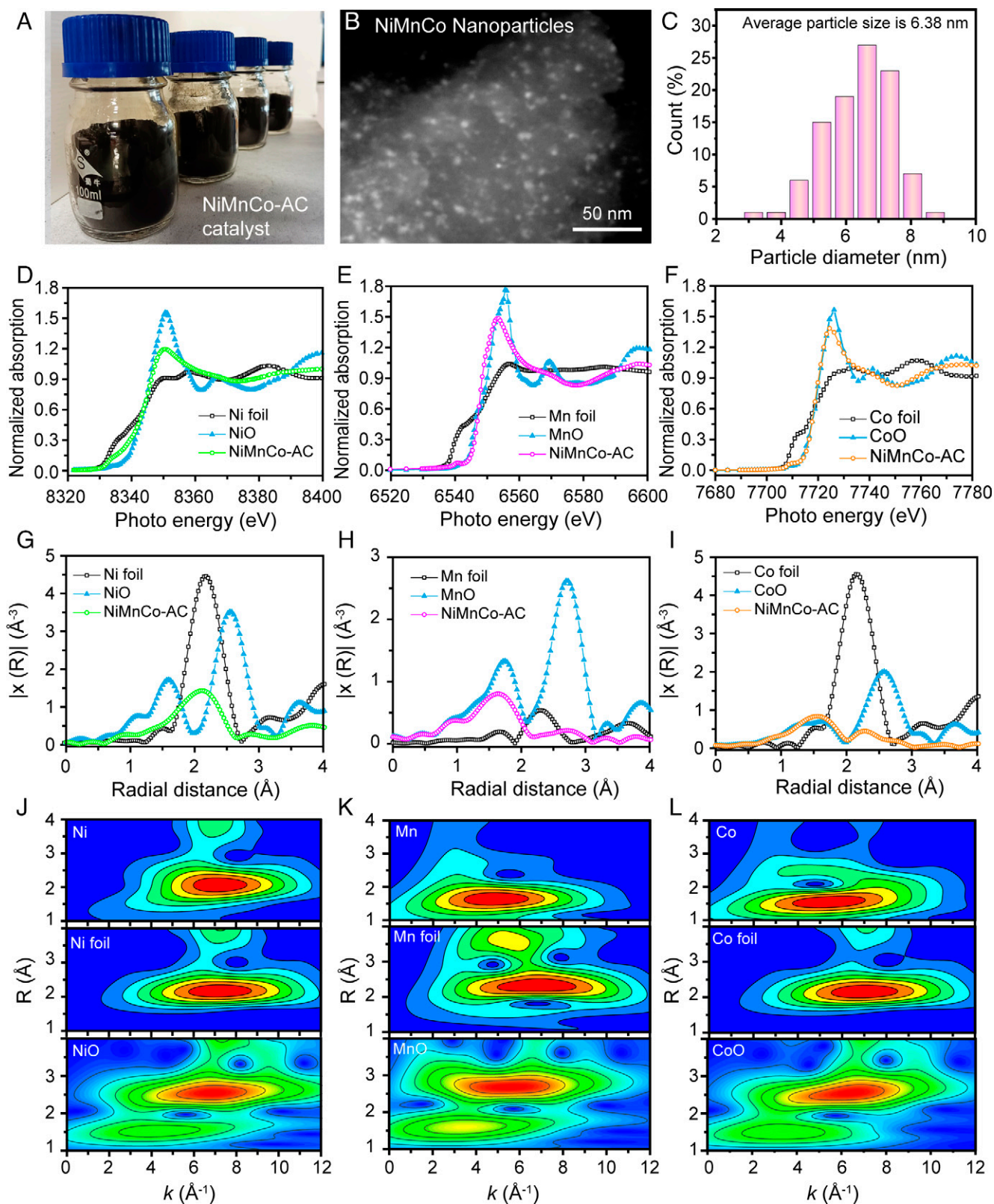
Fig. 2. Morphology and XAFS results of the NiMnCo-AC catalyst. (*A*) The digital image of the NiMnCo-AC catalyst powders. (*B*) High-angle annular dark field image of the NiMnCo-AC catalyst. (*C*) Particle-size distribution of the NiMnCo nanoparticles in the NiMnCo-AC catalyst. (*D–F*) X-ray absorption near-edge spectroscopy curves of the NiMnCo-AC catalyst. (*G–I*) k^2-weighted R-space EXAFS curves of the NiMnCo-AC catalyst. (*J–L*) WT of Ni foil, Mn foil, Co foil, NiO, MnO, CoO, and NiMnCo-AC catalyst (Ni, Mn, and Co).

Co atoms might be the reactive sites. In *SI Appendix,* Figs. S7 and S8, the adsorption calculations results show that O_2 prefers to bond with Mn and Co atoms in a bridge style on the surface of Ni(111)@NiMnCoO$_4$(110), and the adsorption Gibbs free

energy of both O_2 and OH− become lower, indicating that Ni(111)@NiMnCoO$_4$(110) is a potential bifunctional ORR/OER catalyst. According to the adsorption Gibbs free energy (ΔG) diagrams (Fig. 4 *I* and *J* and *SI Appendix,* Fig. S9), Mn
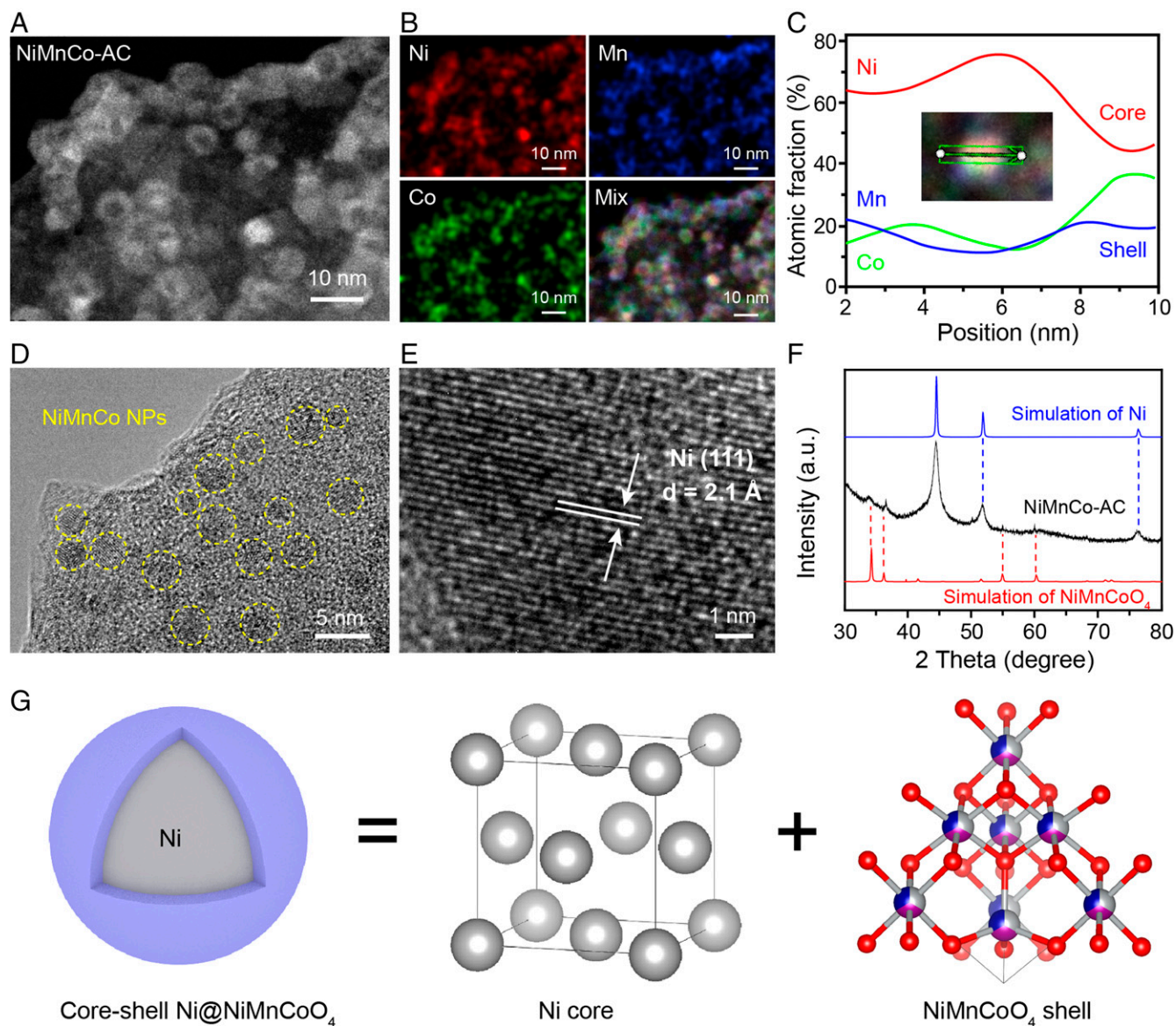
Fig. 3. Morphology and structure analysis of the NiMnCo-AC catalyst. (*A–C*) STEM image, energy dispersive spectrometer mapping images, and line-scan profiles of the NiMnCo-AC catalyst. (*D* and *E*) HRTEM images of the NiMnCo-AC catalyst. (*F*) XRD pattern of the NiMnCo-AC. (*G*) Identified core-shell structure of the NiMnCo nanoparticle.

sites show lower overpotential for both ORR and OER than that of Co sites; therefore, the Mn sites are the main active sites for the Ni(111)@NiMnCoO₄(110) catalyst. The desorption of OH is the rate-determining step for the ORR process, while the formation of *OOH is the rate-determining step for the OER process. Combined with the experimental and calculation results, the NiMnCo-AC catalyst with unique core-shell structure presents excellent bifunctional electrocatalytic performance.

To evaluate the electrochemical performance of the NiMnCo-AC catalyst in ZABs, a primary ZAB was assembled with the NiMnCo-AC as air-cathode and the zinc plate as anode, as shown in *SI Appendix*, Fig. S10*A*. The electrolyte of 6 M KOH and 0.2 M ZnAc₂ mixed solution was filled into the battery and cycle driven by a peristaltic pump, and the ZAB with NiMnCo-AC shows a high open-circuit voltage (OCV) of 1.43 V (Fig. 5*A*, *Inset*). As shown in Fig. 5*A*, the OCV of NiMnCo-AC is stable at 1.42 V at the initial 3 h, higher than that of the control samples Co-AC (1.40 V), NiMnCoO₄-AC (1.40 V), and PtC/ IrO₂ (1.41 V), which is attributed to the high ORR/OER catalytic activity of the NiMnCo-AC. As depicted in Fig. 5*B*, the

NiMnCo-AC delivers the highest discharge voltages of 1.33, 1. 32, 1.30, 1.27, 1.23, 1.14, and 1.02 V at the current densities of 1, 2, 5, 10, 20, 50, and 100 mA cm⁻², respectively. When the current densities are recovered to 5 and 2 mA cm⁻², the discharge voltages of NiMnCo-AC are recovered to 1.28 and 1.31 V, respectively, illustrating excellent rate performance and good stability of the ZAB with NiMnCo-AC cathode. A blue LED was powered with two or three primary ZABs in series, displaying the potential applications of ZAB with NiMnCo-AC (Fig. 5*C* and *SI Appendix*, Fig. S10*B*). In Fig. 5*D*, the ZAB with NiMnCo-AC delivers stable discharge voltages of 1.19, 1.16, and 1.05 V after long discharges of 281, 151, and 57 h at the current densities of 10, 20, and 50 mA cm⁻², respectively, which is attributed to the high catalytic activity and good stability of the NiMnCo-AC catalyst. The specific discharge capacities of ZAB with the NiMnCo-AC cathode were calculated to be 794, 784, and 779 mAh g⁻¹ at the current density of 10, 20, and 50 mA cm⁻², respectively, which are 96, 95, and 94% of the theoretical specific capacity (*SI Appendix*, Fig. S11). The comparison of long discharge curves of ZABs with NiMnCo-
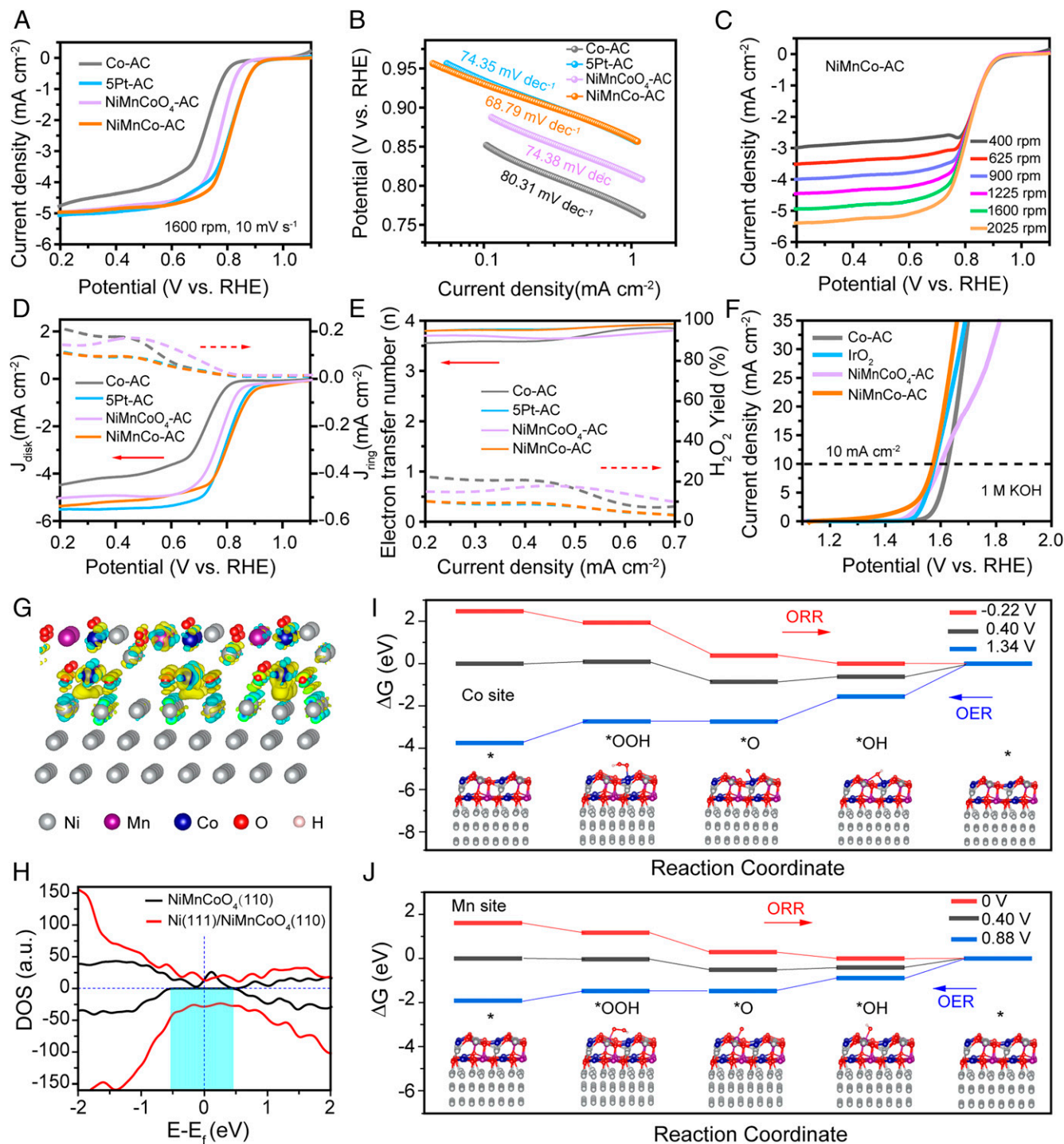
Fig. 4. The electrocatalytic performance of the NiMnCo-AC catalyst. (*A*) ORR polarization curves of the Co-AC, NiMnCo-AC, NiMnCoO$_4$-AC, and 5Pt-AC catalysts. (*B*) Tafel plots derived from the ORR curves. (*C*) ORR curves of the NiMnCo-AC catalyst in 0.1 M KOH with increasing rotating rates from 400 to 2,025 rpm. (*D*) RRDE curves of the Co-AC, NiMnCo-AC, NiMnCoO$_4$-AC, and 5Pt-AC catalysts. (*E*) Percentage of peroxide production and the electron transfer number based on the RRDE results. (*F*) OER polarization curves of the Co-AC, NiMnCo-AC, NiMnCoO$_4$-AC, and IrO$_2$ catalysts in 1 M KOH at the rotating rate of 1,600 rpm. (*G*) Interfacial electron transfer in Ni(111)@NiMnCoO$_4$(110). Yellow and cyan iso-surface represents electron accumulation and electron depletion; the iso-surface value is 0.01 e Å^{-3}. (*H*) The DOS on NiMnCoO$_4$(110) and Ni(111)@NiMnCoO$_4$(110). (*I* and *J*), Gibbs free energy diagrams of ORR/OER on the Co sites (*I*) and Mn sites (*J*) of Ni(111)@NiMnCoO$_4$(110).

AC, Co-AC, NiMnCoO$_4$-AC, and PtC/IrO$_2$ are shown in *SI Appendix*, Fig. S12, and the NiMnCo-AC sample demonstrates the highest discharge voltage and specific capacity at the current density of 50 mA cm^{-2}.

As shown in Fig. 5*E*, the ZAB with NiMnCo-AC presents the lowest voltage gap pf 0.72 V at the initial three charge and discharge processes at 10 mA cm^{-2}, better than that with the Co-AC catalyst (0.87 V), NiMnCoO$_4$-AC catalyst (0.87 V),

and commercial PtC/IrO$_2$ catalyst (0.76 V). The long-term cycling stability of ZABs with Co-AC, NiMnCo-AC, NiMn-CoO$_4$-AC, and PtC/IrO$_2$ catalysts were assessed by galvanostatic charge and discharge at the current density of 10 mA cm^{-2}. The ZAB with NiMnCo-AC is cycled for 200 h without obvious voltage decay, while the commercial PtC/IrO$_2$ deteriorated rapidly after 30 h (Fig. 5*F*). The excellent cycling stability of NiMnCo-AC is benefited from good reversibility of the
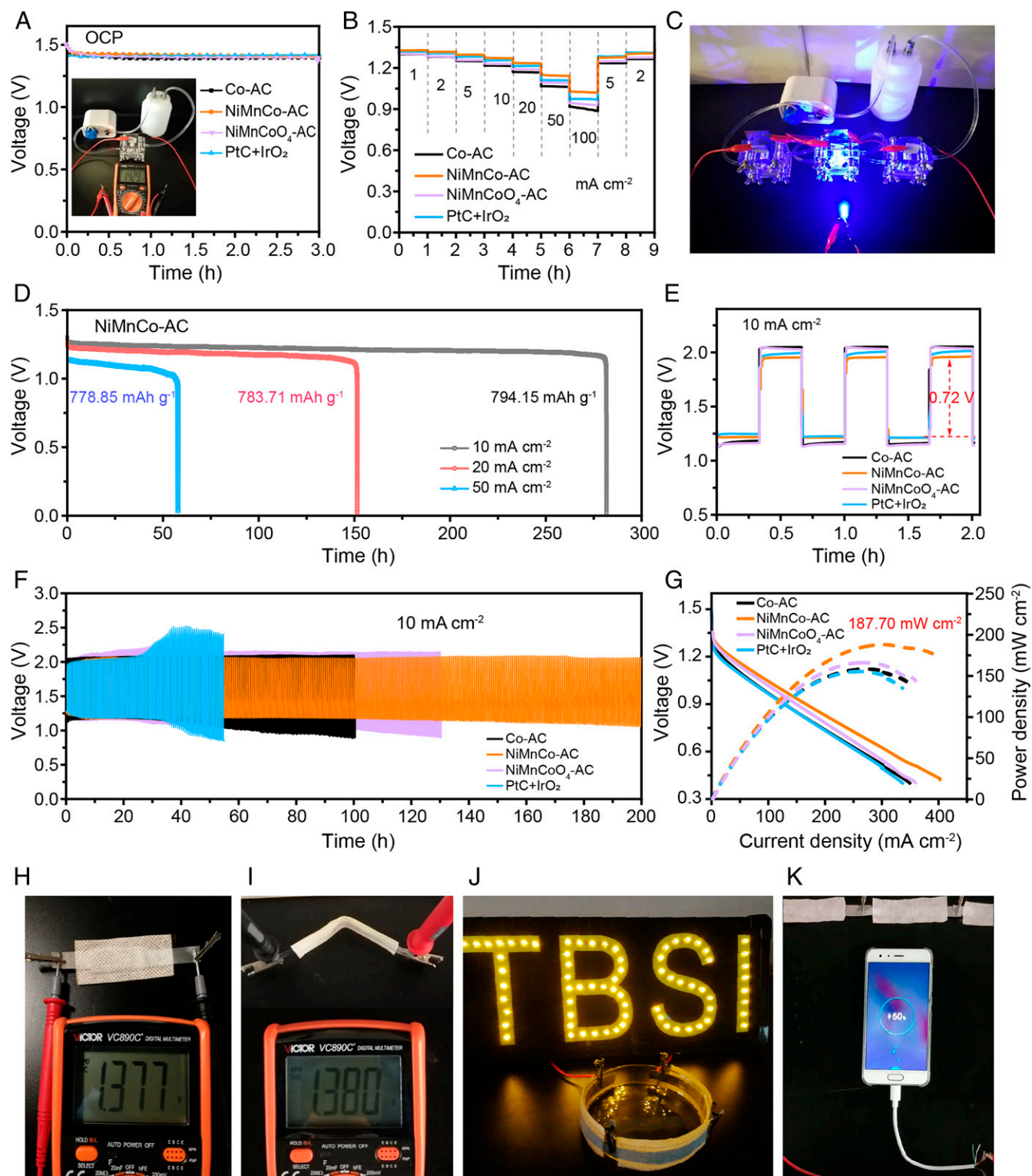
Fig. 5. The electrochemical performance of ZABs with Co-AC, NiMnCo-AC, NiMnCoO₄-AC, and PtC/IrO₂ cathodes. (*A*) The open-circuit potential of primary ZABs at the initial 3 h. (*Inset*) Setup of the primary ZAB with NiMnCo-AC. The OCV was detected to be 1.429 V by a multimeter. (*B*) Discharge curves of ZABs at various current densities. (*C*) A blue LED was powered by three series-connected ZABs. (*D*) Long discharge curves of ZABs with NiMnCo-AC at the current densities of 10, 20, and 50 mA cm^{-2}. (*E*) The initial three charge–discharge curves of ZABs at the current density of 10 mA cm^{-2}. (*F*) Cycling performance of ZABs at the current density of 10 mA cm^{-2}. (*G*) The *i-v* polarization and power density curves of ZABs. (*H* and *I*) The OCV of flexible ZABs with NiMnCo-AC at original and bending circumstances. (*J*) An LED light with TBSI (Tsinghua-Berkeley Shenzhen Institute) signal was powered by three series-connected flexible ZABs. (*K*) Demonstration of charging smartphone by three series-connected flexible ZABs.

NiMnCo-AC cathode in ZAB, which is inherited from the outstanding bifunctional ORR/OER performance of the NiMnCo-AC catalyst. In the *i-v* polarization curves and the corresponding power density curves (Fig. 5*G*), the ZAB with NiMnCo-AC

exhibits the maximum power density of 187.7 mW cm^{-2}, which is 32.7 mW cm^{-2} higher than that of commercial PtC/IrO₂ (*SI Appendix*, Fig. S13), illustrating the high catalytic activity of the NiMnCo-AC cathode. To further explore the potential

applications, a flexible ZAB was assembled with NiMnCo-AC as cathode, zinc foil as anode, and polyvinyl alcohol-KOH film as gel electrolyte. As demonstrated in Fig. 5 *H* and *I*, the flexible ZAB exhibits OCVs of 1.377 and 1.380 V at the original and bending circumstances, respectively. Three series-connected flexible ZABs can power an LED scroller with TBSI signal at the curved state (Fig. 5*J*). Moreover, three series-connected flexible ZABs can charge a smartphone, as shown in Fig. 5*K*, revealing the potential applications of the flexible ZABs.

Conclusions. In this work, we developed a rapid thermal radiation method to convert spent NMC cathodes in LIBs to NiMnCo-AC catalysts through acid leaching and radiative heating, which can not only avoid the sophisticated separation processes during the recycling of spent LIBs, but also efficiently synthesize the NiMnCo-AC catalyst with high catalytic activity to both ORR and OER. EXAFS and XRD simulation results illustrate that the NiMnCo-AC catalyst has a core-shell structure with fcc Ni in the core and spinel $NiMnCoO_4$ in the shell. Theoretical calculations and electrochemical measurements revealed a low energy barrier of the NiMnCo-AC in ORR/OER process due to the electronic structure redistribution caused by the Ni core and effective active sites on the NiMnCoO$_4$ shell, ensuring high electrocatalytic activities of the NiMnCo-AC catalyst. The NiMnCo-AC cathode also presents high electrochemical performance in ZABs, such as the high power density of 187.7 mW cm^{-2}, low voltage gap of 0.72 V at the initial three cycles, and long cycling duration of 200 h at the current density of 10 mA cm^{-2}. Therefore, the rapid thermal radiation method to fabricate highly efficient transition metal catalysts from used LIBs paves an interesting way to reuse spent LIBs as ZABs.

Materials and Methods

Preparation of the NiMnCo-AC Precursor from a Spent NMC532 Cathode. The spent LIBs with a NMC cathode were disassembled in water. The cathodes were immersed into an *N*-methyl-2-pyrrolidone solvent to dissolve the poly(vinylidene fluoride) binder, and after drying, the black powders of NMC cathodes were collected. After adding the black powders into 1 M oxalic acid, the solution was heated to 95 °C and kept for 3 h under continuous stirring. The lithium ions were dissolved into the oxalic acid solution, while the Ni, Mn, and Co were precipitated into oxalate salts. The precipitates were dissolved into a nitric acid, and a mixed NiMnCo solution was obtained after removing the carbon black and other insoluble impurities through filtration. The concentration of the NiMnCo mixed solution was determined by ICP-OES measurement. A certain amount of the mixed NiMnCo solution was loaded onto activated carbon support (coconut shell–based activated carbon) with a mass loading of NiMnCo ~2 wt%. Then, the NiMnCo-AC precursor was obtained after drying at 50 °C for 24 h.

Preparation of the NiMnCo-AC Catalyst through the Rapid Thermal Radiation Method. The rapid thermal radiation was conducted in a homemade argon-filled reactor. The carbon cloth was used as a thermal radiation source, which can be heated to 2,000 K by an external direct current power source. The obtained NiMnCo-AC precursor was transferred onto a carbon cloth and moved across a joule heating source at a high temperature (2,000 K) with a moving speed of 0.5 cm s^{-1}. The NiMnCo salt was decomposed into NiMnCo nanoparticles after the rapid thermal radiation and uniformly dispersed on the surface of active carbon support, which is named NiMnCo-AC catalyst. The contrast Co-AC sample was synthesized through the same method from the spent $LiCoO_2$ cathode material. H_2PtCl_6 was used as the precursor for the synthesis of the 5Pt-AC sample. The NiMnCoO$_4$-AC sample was obtained by oxidizing the NiMnCo-AC catalyst at 240 °C for 3 h.

Characterization. The morphology of the NiMnCo-AC catalyst was characterized by a FEI Titan Cube Themis G2 300 TEM. ICP-OES was conducted on an Agilent 5110. The N_2 adsorption/desorption isotherm was measured at 77 K through the Micrometrics ASAP2460 instrument. The XRD patterns were tested by a Bruker D8 using a Cu Kα radiation source with the scan rate of 2.5° min^{-1} at 40 kV and 40 mA. The X-ray absorption measurement was conducted on BL1W1B station in Beijing Synchrotron Radiation Facility. The Ni foil, Mn foil, and Co foil were used to calibrate the energy for the Ni K edge, Mn K edge, and Co K edge, respectively. The obtained XAFS results were processed by ATHENA to substrate the background and normalize the data, and ARTEMIS software was employed to obtain the local structure of the samples by fitting the EXAFS data.

Electrocatalytic Measurements. Electrocatalytic performance of the catalysts was evaluated on a CHI 760E electrochemical workstation. See *SI Appendix* for detailed information.

Electrochemical Performance of ZABs. The rechargeable ZABs were assembled into a homemade device, and the electrochemical performance was measured on a Land CT2001 A battery test system. The polarization curves of ZABs were measured on a CHI 760E electrochemical workstation. See *SI Appendix* for detailed information.

DFT Calculation. All the computations were performed by means of spin-polarized DFT methods with the Perdew–Burke–Ernzerhof (PBE) exchange correlation functional using the Vienna Ab-initio Simulation Package (VASP) code (37). Please see the detailed information in *SI Appendix*.

Data Availability. All study data are included in the article and/or *SI Appendix*.

1. E. Fan et al., Sustainable recycling technology for li-ion batteries and beyond: Challenges and future prospects. *Chem. Rev.* **120**, 7020–7063 (2020).
2. G. Harper et al., Recycling lithium-ion batteries from electric vehicles. *Nature* **575**, 75–86 (2019).
3. X. Zheng et al., A mini-review on metal recycling from spent lithium ion batteries. *Engineering* **4**, 361–370 (2018).
4. B. Chen et al., Efficient reversible conversion between MoS$_2$ and Mo/Na$_2$ S enabled by graphene-supported single atom catalysts. *Adv. Mater.* **33**, e2007090 (2021).
5. N. Vieceli, R. Casasola, G. Lombardo, B. Ebin, M. Petranikova, Hydrometallurgical recycling of EV lithium-ion batteries: Effects of incineration on the leaching efficiency of metals using sulfuric acid. *Waste Manag.* **125**, 192–203 (2021).
6. X. Zhang et al., Toward sustainable and systematic recycling of spent rechargeable batteries. *Chem. Soc. Rev.* **47**, 7239–7302 (2018).
7. J. J. Roy, B. Cao, S. Madhavi, A review on the recycling of spent lithium-ion batteries (LIBs) by the bioleaching approach. *Chemosphere* **282**, 130944 (2021).
8. Y. Shi, M. Zhang, Y. S. Meng, Z. Chen, Ambient-pressure relithiation of degraded Li$_x$Ni$_{0.5}$Co$_{0.2}$Mn$_{0.3}$O$_2$(0 < x < 1) via eutectic solutions for direct regeneration of lithium-ion battery cathodes. *Adv. Energy Mater.* **9**, 1900454 (2019).
9. X. Zeng, J. Li, B. Shen, Novel approach to recover cobalt and lithium from spent lithium-ion battery using oxalic acid. *J. Hazard. Mater.* **295**, 112–118 (2015).
10. M. Chen et al., Recycling end-of-life electric vehicle lithium-ion batteries. *Joule* **3**, 2622–2646 (2019).
11. M. Fan, X. Chang, Q. Meng, L. J. Wan, Y. G. Guo, Progress in the sustainable recycling of spent lithium-ion batteries. *SusMat* **1**, 241–254 (2021).
12. Q. Li, K. Y. Fung, K. M. Ng, Separation of Ni, Co, and Mn from spent LiNi$_{0.5}$Mn$_{0.3}$Co$_{0.2}$O$_2$ cathode materials by ammonia dissolution. *ACS Sustain. Chem.& Eng.* **7**, 12718–12725 (2019).
13. G. Lombardo et al., Comparison of the effects of incineration, vacuum pyrolysis and dynamic pyrolysis on the composition of NMC-lithium battery cathode-material production scraps and separation of the current collector. *Resour. Conserv. Recycling* **164**, 105142 (2021).
14. T. Or, S. W. D. Gourley, K. Kaliyappan, A. Yu, Z. Chen, Recycling of mixed cathode lithium-ion batteries for electric vehicles: Current status and future outlook. *Carbon Energy* **2**, 6–43 (2020).
15. M. K. Tran, M.-T. F. Rodrigues, K. Kato, G. Babu, P. M. Ajayan, Deep eutectic solvents for cathode recycling of Li-ion batteries. *Nat. Energy* **4**, 339–345 (2019).
16. B. Cui et al., Waste to wealth: Defect-rich Ni-incorporated spent LiFePO$_4$ for efficient oxygen evolution reaction. *Sci. China Mater.* **64**, 2710–2718 (2021).
17. B. He, Study on the preparation and modification of LiNi$_{0.6}$Co$_{0.2}$Mn$_{0.2}$O$_2$ from spent lithium ion batteries as lithium and cobalt source. *Int. J. Electrochem. Sci.* **15**, 6920–6929 (2020).
18. S. S. Shinde et al., Ampere-hour-scale zinc-air pouch cells. *Nat. Energy* **6**, 592–604 (2021).
19. M. Wu et al., Defect electrocatalysts and alkaline electrolyte membranes in solid-state zinc-air batteries: Recent advances, challenges, and future perspectives. *Small Methods* **5**, e2000868 (2021).
20. Q. Wang et al., Facile synthesis of ternary spinel Co-Mn-Ni nanorods as efficient bi-functional oxygen catalysts for rechargeable zinc-air batteries. *J. Power Sources* **435**, 226761 (2019).

21. W.-S. Chen, H.-J. Ho, Recovery of valuable metals from lithium-ion batteries NMC cathode waste materials by hydrometallurgical methods. *Metals (Basel)* **8**, 321 (2018).
22. R. Sommerville *et al.*, A qualitative assessment of lithium ion battery recycling processes. *Resour. Conserv. Recycling* **165**, 105219 (2021).
23. F. Larouche *et al.*, Progress and status of hydrometallurgical and direct recycling of li-ion batteries and beyond. *Materials (Basel)* **13**, 801 (2020).
24. B. Makuza, Q. Tian, X. Guo, K. Chattopadhyay, D. Yu, Pyrometallurgical options for recycling spent lithium-ion batteries: A comprehensive review. *J. Power Sources* **491**, 229622 (2021).
25. X. Hu, E. Mousa, Y. Tian, G. Ye, Recovery of Co, Ni, Mn, and Li from Li-ion batteries by smelting reduction - Part I: A laboratory-scale study. *J. Power Sources* **483**, 228936 (2021).
26. M. Sethurajan *et al.*, Recent advances on hydrometallurgical recovery of critical and precious elements from end of life electronic wastes–A review. *Crit. Rev. Environ. Sci. Technol.* **49**, 212–275 (2019).
27. W. Lv *et al.*, A Critical Review and Analysis on the Recycling of Spent Lithium-Ion Batteries. *ACS Sustain. Chem.& Eng.* **6**, 1504–1521 (2018).
28. W. Xuan, A. Otsuki, A. Chagnes, Investigation of the leaching mechanism of NMC 811 ($LiNi_{0.8}Mn_{0.1}Co_{0.1}O_2$) by hydrochloric acid for recycling lithium ion battery cathodes. *RSC Advances* **9**, 38612–38618 (2019).
29. J. Wang *et al.*, Recycling lithium cobalt oxide from its spent batteries: An electrochemical approach combining extraction and synthesis. *J. Hazard. Mater.* **405**, 124211 (2021).
30. H. Ali, H. A. Khan, M. G. Pecht, Circular economy of Li batteries: Technologies and trends. *J. Energy Storage* **40**, 102690 (2021).
31. Y. Liu *et al.*, Electrochemical tuning of olivine-type lithium transition-metal phosphates as efficient water oxidation catalysts. *Energy Environ. Sci.* **8**, 1719–1724 (2015).
32. J. Wang *et al.*, Redirecting dynamic surface restructuring of a layered transition metal oxide catalyst for superior water oxidation. *Nat. Catal.* **4**, 212–222 (2021).
33. Z. Lu *et al.*, Electrochemical tuning of layered lithium transition metal oxides for improvement of oxygen evolution reaction. *Nat. Commun.* **5**, 4345 (2014).
34. Z. Lu *et al.*, Identifying the active surfaces of electrochemically tuned $LiCoO_2$ for oxygen evolution reaction. *J. Am. Chem. Soc.* **139**, 6270–6276 (2017).
35. Y. Gershinsky, D. Zitoun, Direct chemical synthesis of lithium sub-stochiometric olivine $Li_{0.7}Co_{0.75}Fe_{0.25}PO_4$ coated with reduced graphene oxide as oxygen evolution reaction electrocatalyst. *ACS Catal.* **8**, 8715–8725 (2018).
36. S. Zhang *et al.*, Spontaneous delithiation under operando condition triggers formation of an amorphous active layer in spinel cobalt oxides electrocatalyst toward oxygen evolution. *ACS Catal.* **9**, 7389–7397 (2019).
37. G. Kresse, J. Furthmuller, Efficiency of Ab-initio total energy calculations for metals and semiconductors using a plane-wave basis set. *Comput. Mater. Sci.* **6**, 15–50 (1996).